








Spin dynamics in the square-lattice cupola system $\text{Ba}(\text{TiO})\text{Cu}_4(\text{PO}_4)_4$

Luc Testa ^{1,*}, Peter Babkevich,¹ Yasuyuki Kato ², Kenta Kimura ³, Virgile Favre,¹ Jose A. Rodriguez-Rivera,^{4,5} Jacques Ollivier,⁶ Stéphane Raymond ⁷, Tsuyoshi Kimura ³, Yukitoshi Motome ², Bruce Normand ^{1,8} and Henrik M. Rønnow^{1,†}

¹*Institute of Physics, Ecole Polytechnique Fédérale de Lausanne (EPFL), CH-1015 Lausanne, Switzerland*

²*Department of Applied Physics, University of Tokyo, Hongo, Tokyo 113-8656, Japan*

³*Department of Advanced Materials Science, University of Tokyo, Kashiwa, Chiba 277-8561, Japan*

⁴*NIST Center for Neutron Research, National Institute of Standards and Technology, Gaithersburg, Maryland 20899, USA*

⁵*Materials Science and Engineering Department, University of Maryland, College Park, Maryland 20742, USA*

⁶*Institut Laue-Langevin, Boîte Postale 156, 38042 Grenoble Cedex 9, France*

⁷*Université Grenoble Alpes, CEA, IRIG, MEM, MDN, 38000 Grenoble, France*

⁸*Paul Scherrer Institute, CH-5232 Villigen PSI, Switzerland*



(Received 1 March 2022; revised 13 May 2022; accepted 16 May 2022; published 6 June 2022)

We report high-resolution single-crystal inelastic neutron scattering measurements on the spin-1/2 antiferromagnet $\text{Ba}(\text{TiO})\text{Cu}_4(\text{PO}_4)_4$. This material is formed from layers of four-site “cupola” structures, oriented alternately upwards and downwards, which constitute a rather special realization of two-dimensional (2D) square-lattice magnetism. The strong Dzyaloshinskii-Moriya (DM) interaction within each cupola, or plaquette, unit has a geometry largely unexplored among the numerous studies of magnetic properties in 2D Heisenberg models with spin and spatial anisotropies. We have measured the magnetic excitations at zero field and in fields up to 5 T, finding a complex mode structure with multiple characteristic features that allow us to extract all the relevant magnetic interactions by modeling within the linear spin-wave approximation. We demonstrate that $\text{Ba}(\text{TiO})\text{Cu}_4(\text{PO}_4)_4$ is a checkerboard system with almost equal intra- and interplaquette couplings, in which the intraplaquette DM interaction is instrumental both in enforcing robust magnetic order and in opening a large gap at the Brillouin-zone center. We place our observations in the perspective of generalized phase diagrams for spin-1/2 square-lattice models and materials, where exploring anisotropies and frustration as routes to quantum disorder remains a frontier research problem.

DOI: [10.1103/PhysRevB.105.214406](https://doi.org/10.1103/PhysRevB.105.214406)

I. INTRODUCTION

Despite its apparent simplicity, the antiferromagnetic (AF) spin-1/2 Heisenberg model encapsulates all the rich many-body physics of noncommuting quantum variables. Even on a one-dimensional (1D) chain with only nearest-neighbor interactions, its exact solution describes a strongly fluctuating spin state with fractionalized excitations [1–3]. On the square lattice in 2D, the nearest-neighbor (J_1) model shows spontaneous breaking of the continuous spin symmetry and Néel-type magnetic order [4,5], albeit with a quantum renormalization of the ordered moment to 61% of its maximal value [6]. The idea that quantum fluctuations could destroy this order in 2D was put forward originally for the triangular lattice [7], on which AF interactions are geometrically frustrated. While the concept of the resonating valence bond (RVB) state was not realized on this lattice, it returned to prominence in the context of cuprate superconductivity [8], and it is a leading candidate for the ground state of the square lattice frustrated by diagonal next-nearest-neighbor (J_2) interactions [9]. In this sense, frustrated

2D Heisenberg models are the original prototype for quantum spin-liquid states [10].

The study of more complex square-lattice quantum antiferromagnets has been pursued in a number of directions in recent years. In the direction of frustration, both analytical and numerical studies of the J_1 - J_2 model [11–17] have reached a very high level of sophistication without reaching a consensus on the nature of the quantum disordered phases around $J_2 = J_1/2$. In the direction of spatial anisotropy, numerical investigation of plaquette-based, or tetramerized, square lattices with no frustration reveals a quantum phase transition (QPT) to a plaquette-singlet state at an inter- to intraplaquette coupling ratio $\alpha = 0.55$ [18,19]. A further development of spatial anisotropy and frustration is the checkerboard, or “2D pyrochlore” lattice [20,21], which also exhibits a QPT to quantum disorder as a function of J_2/J_1 . In the direction of spin anisotropies, Dzyaloshinskii-Moriya (DM) interactions [22,23] are the leading consequence of broken bond-inversion symmetry in materials but, despite their ubiquity, they have seen rather little attention in square-lattice geometries; available studies concern spin ladders [24], tetramer systems with pyrochlore geometry [25], and coupled chains treated by the simplification of staggered magnetic fields [26]. Recent numerical work has explored some of the

*luc.testa@gmail.com

†henrik.ronnow@epfl.ch

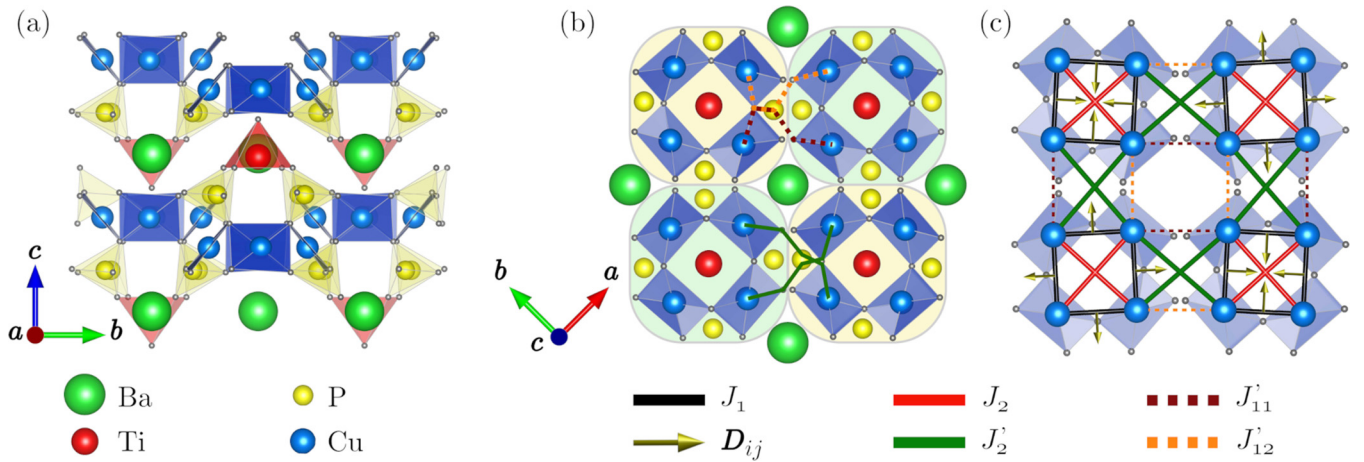


FIG. 1. Schematic representation of the structure of Ba(TiO)Cu₄(PO₄)₄, showing Cu (blue), Ba (green), Ti (red), P (yellow), and O (gray) atoms with associated coordination polyhedra. (a) Projection on the *bc* plane, providing a side view of the buckled layers. (b) Projection on the *ab* plane of the layers, highlighting the square cupola structures as four CuO₄ squares (blue) connected around a Ti atom. Yellow and green shading indicate, respectively, upward- and downward-oriented cupolas. (c) Representation of the square-planar (*ab*) magnetic lattice, meaning the interactions between Cu atoms defined in Eq. (1). Figure 2 provides perspective views of the cupola structures and the resulting geometry of the DM vectors, D_{ij} .

parameter space for frustrated square lattices with exchange anisotropies [27].

Experimentally, the monolayer insulating parent cuprate La₂CuO₄ has been used to obtain accurate measurements of the quantum corrections to the spin-wave description of the nearest-neighbor square-lattice model [28]. However, the high energy scales of the cuprate materials mean that nontrivial additional physics is involved [29], possibly including terms beyond quantum magnetism. Of the square-lattice compounds with lower energy scales, the most faithful realization is probably copper deuteroformate tetradeuterate (CFTD) [30], in which the dynamical properties have been studied at all temperatures, while the recent discovery of Sr₂CuTeO₆ offers another candidate with a small J_2/J_1 ratio [31]. Beyond the nearest-neighbor square lattice, many compounds have been investigated as possible realizations of the J_2/J_1 model, and while the $AA'VO(PO_4)_2$ vanadium phosphates offer a rich variety of (AA') cation options that affect the coupling ratio [32], they also suffer from a breaking of 90-degree structural symmetry. Perhaps the best realization of the tetramerized square lattice is Na_{1.5}VOPO₄F_{0.5} [33], which opens a route towards experimental studies of plaquette-based systems on the frustrated square lattice, while La₂O₂Fe₂O(Se,S)₂ offers a similar possibility for (“double”) checkerboard geometries [34]. However, most studies to date have focused on the static properties of these materials, and the dynamics of such extended models remain somewhat unexplored.

A series of compounds that is known to realize 2D spin-1/2 antiferromagnetism on the tetramerized square lattice is the $A(BO)Cu_4(PO_4)_4$ family, where (A ; B) = (Ba, Pb, Sr; Ti) and (K; Nb). Cu₄O₁₂ tetramers form cupola structures, represented in Figs. 1 and 2(a), which are linked in the *ab* plane in such a way that upward- and downward-oriented cupolas alternate in a checkerboard pattern. It was shown using polarized-light microscopy and x-ray diffraction that the cupolas also have an alternating rotation about the *c* axis, shown in Figs. 1(b) and 1(c), and that the extent of this struc-

tural chirality depends on the A²⁺ cation [35]. This tuneable crystal structure, which reaches a highly symmetrical configuration in the (K; Nb) compound [36], was found by a range of thermodynamic measurements [36–42] to cause significant changes in the magnetic interactions. In fact, most of these studies were inspired by the magnetoelectric behavior that results from ordering of the magnetic quadrupoles formed on the Cu₄O₁₂ tetramers [37,43], and also leads to nonreciprocal optical properties [44,45]. Efforts to relate these properties to the structure and geometry of the different magnetization measurements [38,39,41,46,47]. Thus the $A(BO)Cu_4(PO_4)_4$ family offers a wealth of options for exploring how the spin dynamics evolve throughout the composition series.

In the present study, we begin this investigation by focusing on Ba(TiO)Cu₄(PO₄)₄. It was reported by previous powder inelastic neutron studies that the excitation spectrum has a robust gap [37], despite the presence of magnetic order, providing an initial hint for the role of DM interactions, which are allowed by the rather low symmetry of the Cu-Cu bond pathways in this compound. Efforts to extract the magnetic exchange parameters have been made on the basis of *ab initio* calculations [37,39], also combined with fitting the high-field magnetization response for different field directions to a cluster mean-field (CMF) approximation [38,41]. These studies suggest a model with dominant intraplaquette interactions, including a strong DM term whose vector direction is of key importance, and they provide a good description of the strong magnetoelectric effect. However, a quantitative benchmarking of the proposed interaction parameters by comparison with the spin excitation spectrum is precluded by the fact that dynamical measurements have to date been possible only with a powder sample [37].

We have performed a high-resolution inelastic neutron scattering (INS) study of single-crystalline Ba(TiO)Cu₄(PO₄)₄. We observe a complex series of magnetic excitations with characteristic periodicities, dispersions,

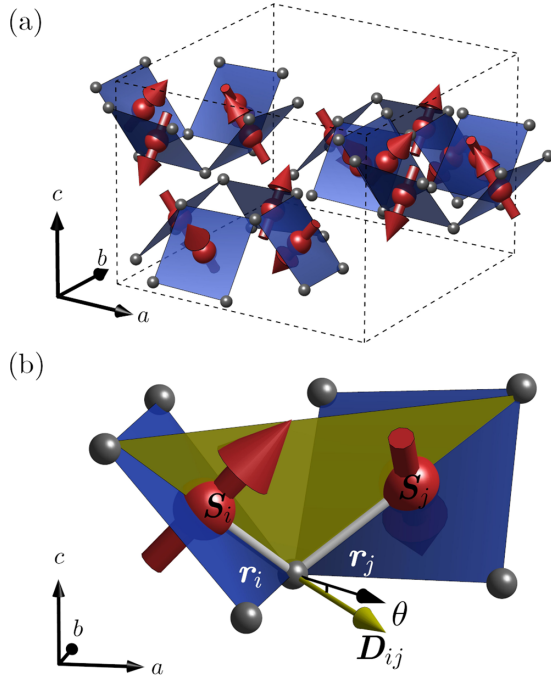


FIG. 2. Schematic representation of the ordered magnetic structure of $\text{Ba}(\text{TiO})\text{Cu}_4(\text{PO}_4)_4$. (a) Ordered moments on each Cu atom (red) are oriented approximately normal to the CuO_4 squares and form a two-in, two-out configuration on each cupola, with the relative directions between upward- and downward-oriented cupolas as shown. (b) The DM vector (yellow) lies in a vertical plane equidistant from the two Cu atoms and forms an angle θ with the horizontal (ab) plane.

splittings, and intensities. From these measurements we determine a definitive set of magnetic interaction parameters that describe the dynamical structure factor to high accuracy. In contrast to the results based on static quantities, we find that the leading interplaquette interaction has a magnitude almost identical to the leading intraplaquette one. We obtain five other subsidiary interactions with high fidelity and stress the sensitivity of our fits to both in- and out-of-plane components of the DM interaction. These results allow us to relate $\text{Ba}(\text{TiO})\text{Cu}_4(\text{PO}_4)_4$ to the ongoing investigation of tetramerized “ J_1 - J'_1 - J_2 - J'_2 ” models in extended square-lattice systems.

The manuscript is organized as follows. Section II presents the atomic and magnetic structure of $\text{Ba}(\text{TiO})\text{Cu}_4(\text{PO}_4)_4$. In Sec. III we describe the single-crystal growth and the experimental procedures used for our INS measurements. Our primary results for the dynamic structure factor at zero field are reported in Sec. IV A and our measurements in applied magnetic fields up to 5 T in Sec. IV B. In Sec. IV C we present a detailed analysis of our data based on the linear spin-wave approximation to the magnetic excitations, from which we deduce the optimal set of interaction parameters describing the physics of $\text{Ba}(\text{TiO})\text{Cu}_4(\text{PO}_4)_4$. In Sec. V we analyze the consequences of these parameters for the magnetization and compare these with high-field measurements covering the three primary symmetry directions. Section VI contains a brief discussion connecting the $A(\text{BO})\text{Cu}_4(\text{PO}_4)_4$ compounds to the

general phase diagram of square-lattice models with spatial (tetramerization) and spin (DM) anisotropy. A summary and conclusion are provided in Sec. VII.

II. CRYSTAL AND MAGNETIC STRUCTURE

$\text{Ba}(\text{TiO})\text{Cu}_4(\text{PO}_4)_4$ has a fascinating and complex crystal structure [35], which we show in detail in Fig. 1. As already noted in Sec. I, groups of four corner-sharing CuO_4 squares form Cu_4O_{12} cupola structures, shown in blue in Figs. 1 and 2. These cupolas are connected by PO_4 tetrahedra into square-lattice layers in the (ab) plane, where both their c -axis orientation (up- or down-pointing) and a chirality-inducing rotation about the c axis [Fig. 1(c)] alternate. Together with the TiO_5 pyramids, the PO_4 tetrahedra form a nonmagnetic layer separating the cupola planes [Fig. 1(a)]. This tetragonal chiral structure is well described by the $P4_212$ space group, with lattice parameters $a = 9.60 \text{ \AA}$ and $c = 7.12 \text{ \AA}$. There are eight equivalent magnetic atoms in the crystallographic unit cell (Cu, $S = 1/2$), whose locations can be generated from original position $(0.27, 0.99, 0.40)$.

Initial studies by magnetic neutron diffraction [37] showed the onset of a predominantly antiferromagnetic order below $T_N = 9.5 \text{ K}$, with propagation vector $\mathbf{k} = (0, 0, \frac{1}{2})$ and a large ordered moment of approximately $0.8\mu_B$. Based on this structural and magnetic information, we model the magnetic dynamics of $\text{Ba}(\text{TiO})\text{Cu}_4(\text{PO}_4)_4$ with the Heisenberg Hamiltonian

$$\hat{\mathcal{H}} = \sum_{[i,j]_m} J_m \mathbf{S}_i \cdot \mathbf{S}_j - \sum_{(i,j)} \mathbf{D}_{ij} \cdot (\mathbf{S}_i \times \mathbf{S}_j), \quad (1)$$

where $[i, j]_m$ denotes a sum over relevant Cu-Cu bonds with Heisenberg interactions of strength J_m . Our measurements of the dispersion and intensities of the magnetic excitations (Secs. IV A and IV B) were not previously available, and the aim of our analysis is to identify the relevant magnetic interactions, as represented in Fig. 1(c), and fit the corresponding J_m values (Sec. IV C).

In addition, any understanding of $\text{Ba}(\text{TiO})\text{Cu}_4(\text{PO}_4)_4$ requires DM interactions, and we restrict our considerations to the single term connecting pairs of neighboring Cu sites, (i, j) , within each cupola. By standard structure and symmetry considerations, the DM vectors on the four cupola bonds [Fig. 1(c)] are perpendicular to the vector $\mathbf{r}_i - \mathbf{r}_j$, where \mathbf{r}_i is the bond vector connecting a Cu site to an O atom shared by two CuO_4 squares, and they are oriented at an angle θ to the ab plane, as shown in Fig. 2(b). The presence of a large DM amplitude, $D = |\mathbf{D}|$, and the importance of the angle θ to a detailed understanding of the magnetic order, was suggested in the early studies of Ref. [37]. The DM interaction naturally frustrates the Heisenberg interactions on each cupola and stabilizes a highly noncollinear spin configuration, best understood as a two-in, two-out structure (Fig. 2). The resulting cupola quadrupole moment has been characterized in detail by spherical neutron polarimetry (SNP) [43] and nuclear magnetic resonance (NMR) measurements [48].

III. MATERIAL AND METHODS

Three single crystals of $\text{Ba}(\text{TiO})\text{Cu}_4(\text{PO}_4)_4$ with a total mass of 3.3 g were grown by the flux method [35]. They were coigned on an Al holder to a precision of less than 1° in the $(hk0)$ scattering plane using Laue x-ray diffractometry. Initial measurements of the spin dynamics at zero magnetic field were performed on the MACS spectrometer [49] at NIST and revealed a complex spectrum of modes. However, the energetic resolution available at the selected final wave vector of $k_f = 4.7 \text{ \AA}^{-1}$, obtained with a BeO filter placed before the analyzer, meant that this spectrum could not be resolved completely in parts of the Brillouin zone. To achieve a higher resolution in the required energy ranges, further experiments were performed at zero field on the direct-geometry time-of-flight (TOF) neutron spectrometer IN5 [50], and in a vertical field applied along the sample c axis on the triple-axis spectrometer (TAS) IN12 [51], both at the Institut Laue-Langevin (ILL).

On IN5, measurements were made at 1.5 K in the ordered phase, at 10 K just above T_N , and deep in the paramagnetic phase at 30 K. Inelastic data were collected by rotating the sample around its c axis by a total of 138° , in steps of 1° . Counting times were 20 min per angular step at 1.5 and 30 K, and 13 min per step at 10 K, for a total measurement time of 46 h. The crystals were oriented in order to maximize the accessible range in the $(hk0)$ plane, and such that scattering in the orthogonal direction could be measured using the opening of the orange cryostat. The incident energy was set to $E_i = 7.08 \text{ meV}$ and the chopper rotation speed to 200 Hz, resulting in resolutions of 0.24 meV (FWHM) at the elastic line, decreasing to 0.15 meV (FWHM) at the highest energy transfers. We took advantage of the tetragonal symmetry of $\text{Ba}(\text{TiO})\text{Cu}_4(\text{PO}_4)_4$ by summing the intensities from detection pixels corresponding to momentum transfers, \mathbf{Q} , that are equivalent under crystal symmetry operations of the point group (422). Due to the nondispersive behavior of the excitations along $[0, 0, l]$, the data were integrated over ± 0.6 in l . The TOF data were processed using the HORACE software suite [52].

On IN12, measurements were made at a base temperature of 2 K. The final wave vector was fixed to $k_f = 1.3 \text{ \AA}^{-1}$, giving a resolution of 0.172(5) meV (FWHM). An $80'$ collimator was placed between the monochromator and the sample; the monochromator had both horizontal and vertical focusing while the analyzer was horizontally focused only. The sample was inserted in a 10 T vertical cryomagnet, in which data were collected at field values up to 5 T in 1 T steps. The counting time was 2 min per \mathbf{Q} -point. In both experiments, the intensity $I(\mathbf{Q}, \omega)$ measured at each \mathbf{Q} and energy transfer, ω , is directly proportional to the dynamical structure factor, $S(\mathbf{Q}, \omega)$, convolved with a Gaussian distribution to account for the finite measurement resolution of each spectrometer.

IV. SPIN DYNAMICS

A. Zero applied field

We begin by reporting the INS spectrum of $\text{Ba}(\text{TiO})\text{Cu}_4(\text{PO}_4)_4$ at zero magnetic field, as measured on IN5. Figure 3 presents $I(\mathbf{Q}, \omega)$ at 2 K as color maps of

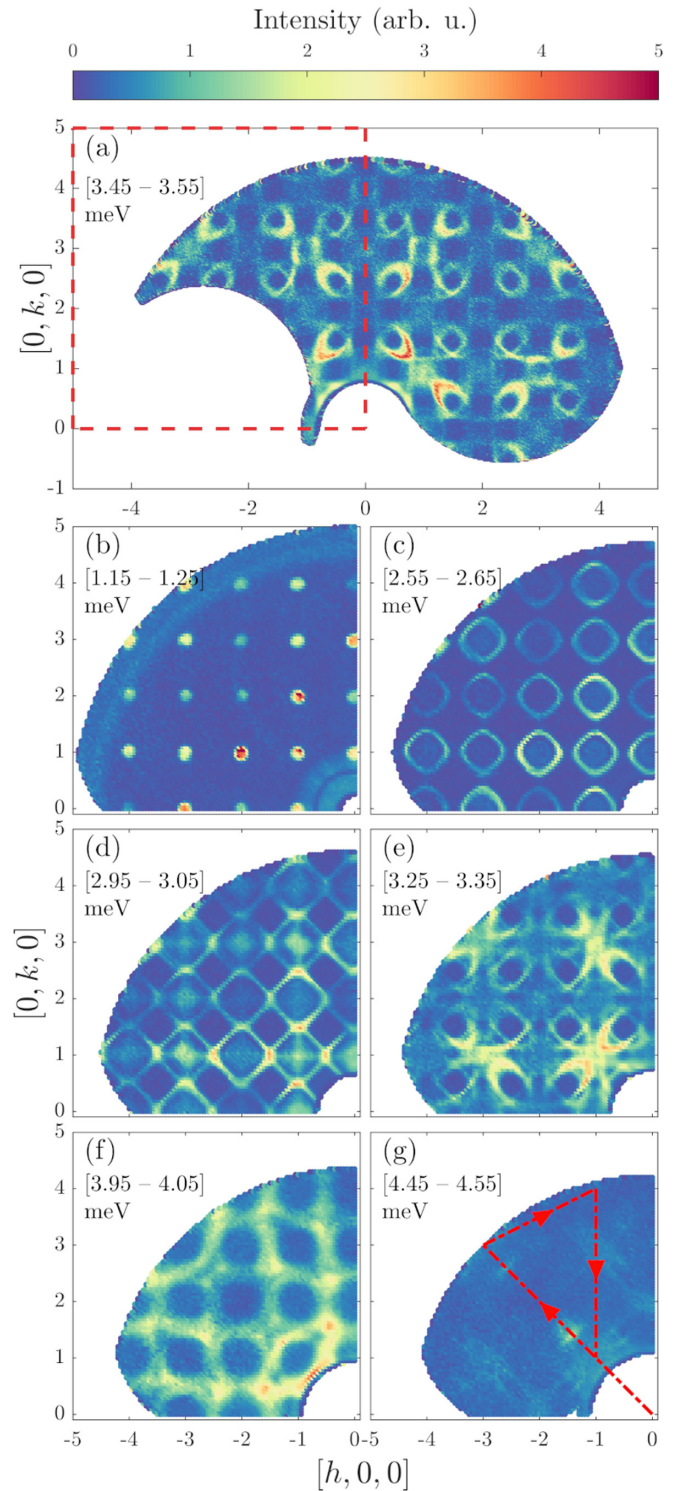


FIG. 3. Scattered intensity, $I(\mathbf{Q}, \omega)$, measured on IN5 at 2 K, integrated over different ω ranges throughout the bandwidth of the excitations, as indicated in each panel, and shown as a function of \mathbf{Q} , in steps of 0.01 \AA^{-1} , in the $(hk0)$ scattering plane. (a) Unsymmetrized data across the full accessible Brillouin zone, highlighting the fourfold symmetry of the excitations in \mathbf{Q} . The dashed red box marks the second quadrant, to which the remaining panels should be referred. (b)–(g) Symmetrized data, folded onto the second quadrant, and shown for six selected energy ranges. Red dashed lines in panel (g) show the scattering wave vectors presented in Fig. 5.

the magnetic excitations integrated over selected constant energy ranges at \mathbf{Q} values spanning several Brillouin zones (BZs). We remark that no phonon excitations are discernible anywhere within the ranges of \mathbf{Q} and ω that we probe.

The format of Fig. 3(a) confirms that the magnetic spectrum has the fourfold symmetry expected from the atomic structure, as may be observed by reflection through and rotation around the origin, which justifies averaging the measured intensity and discussing a single quadrant in the remaining panels. As the energy transfer is increased from zero, Fig. 3(b) shows that gapped spin excitations appear first at the Bragg-peak positions at an energy of 1.13(3) meV. This branch shows a strong dispersion for wave vectors across the BZ [Fig. 3(c)], and at approximately 3 meV they begin to merge while a different excitation branch also emerges at the Bragg peaks [Fig. 3(d)]. In the energy range up to 4 meV, scattering contributions from several different branches disperse and merge, resulting in complicated patterns in \mathbf{Q} [Figs. 3(e) and 3(f)], but ones that always retain the same periodicity. Finally, above 4.4 meV one finds only weak remnant scattering [Fig. 3(g)].

To study the evolution of these spin excitations with ω , Fig. 4 shows representative constant- \mathbf{Q} scans taken along a single high-symmetry direction in reciprocal space. We observe the presence of multiple sharp peaks, all of which are well described by a Gaussian line shape. By extracting peak centers, widths, and intensities in this way, we identify a maximum of seven different excitations in some parts of the BZ. To display this information with maximum clarity, Fig. 5(a) shows the dynamical structure factor, $S(\mathbf{Q}, \omega)$, along several different high-symmetry \mathbf{Q} -space directions.

To describe this extremely rich spectrum, we begin by decomposing the observed excitations into three distinct regimes of energy, which we define on the basis of the $[0, \bar{k}, 0]$ scattering direction (the third panel in Fig. 5). First, there is a robust gap, $\Delta = 1.13(3)$ meV, at the BZ center, and in fact this repeats along all measured directions. Second, a single, sharp excitation branch with a largely cosinusoidal dispersion is present at 1–3 meV, to which we refer henceforth as the low-energy regime. At the BZ boundaries, this mode flattens in a manner reminiscent of a level repulsion with the higher-energy excitations. The gradient with which the low-energy mode disperses around the Bragg-peak positions indicates the magnitude of the leading interaction. The fact that this mode seems to have a periodicity of two BZs [Fig. 3(c) and Fig. 5, third panel] indicates that this interaction spans half of the magnetic unit cell, as may be confirmed from the symmetry [53] of the identical cupola subunits in Fig. 1. Third, the high-energy regime at 3–4.5 meV contains three distinct and continuous modes, one of which merges into the low-energy mode at the lower edge of the energy window. We comment again that there are no magnetic excitations above the upper edge of the high-energy regime [Fig. 3(g)].

We also report a number of subtle details in Fig. 5(a), which are important for different aspects of fitting the relevant interaction parameters. Above the low-energy mode, one may discern the presence of an additional scattering feature with very low intensity; denoting the low-energy mode dispersion

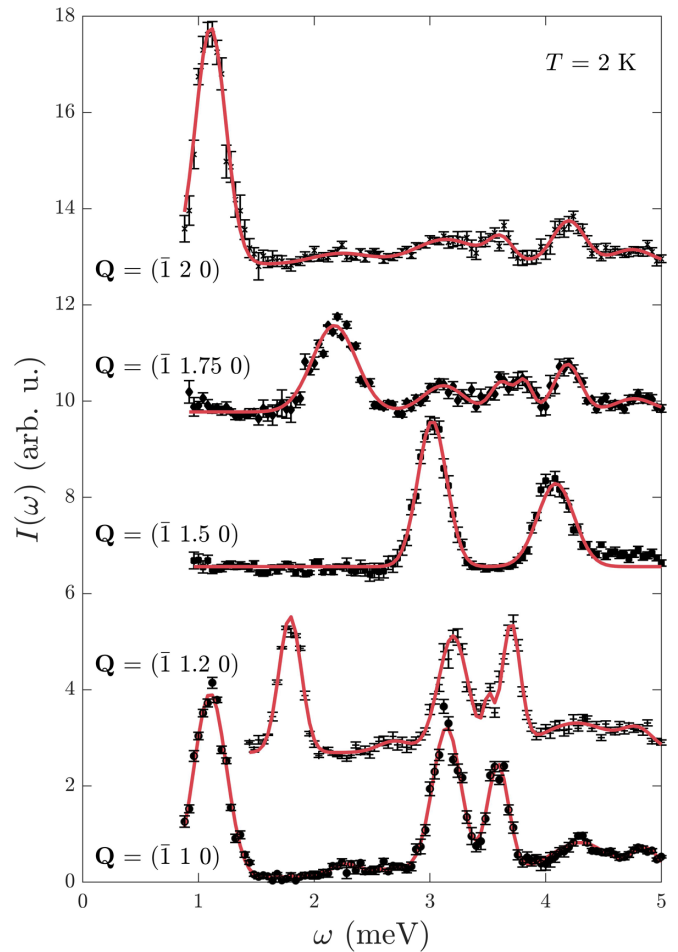


FIG. 4. $I(\mathbf{Q}, \omega)$ (black points) collected on IN5 at 2 K for different \mathbf{Q} points along the $[\bar{1}, k, 0]$ direction and shown as a function of ω . The integration range in the orthogonal direction is $\pm 0.05 \text{ \AA}^{-1}$. The red lines are an interpolated multi-Gaussian fit, from which the peak centers and widths were extracted.

by $E_1(\mathbf{Q})$, this feature appears above $E_{2M}(\mathbf{Q}) = E_1(\mathbf{Q}) + \Delta$. This information allows us to identify the feature as a two-magnon scattering continuum, which is sharpest at its lower boundary, and in Sec. IV B we will obtain further information to confirm this identification. Another important detail is the splitting of the second most energetic mode that we observe around the zone centers, as this is a consequence of the DM interactions and, together with the gap, provides the most accurate means of quantifying D ; this feature, at 3.2–3.5 meV, is clearest for the $[0, \bar{k}, 0]$ direction. In general, the scattering intensity is strongest near the zone centers and in the low-energy regime, although a clear exception occurs in the second BZ, where the high-energy branches are equally intense. We also observe an expected drop in scattering intensity with increasing \mathbf{Q} that arises from the magnetic form factor of Cu. As expected from the crystallographic structure, the magnetic excitations are only very weakly dispersive in the direction orthogonal to the magnetic layers [right panel of Fig. 5(a)], and thus we have chosen to integrate all of our scattered intensities over the range $-0.6 < l < 0.6$.

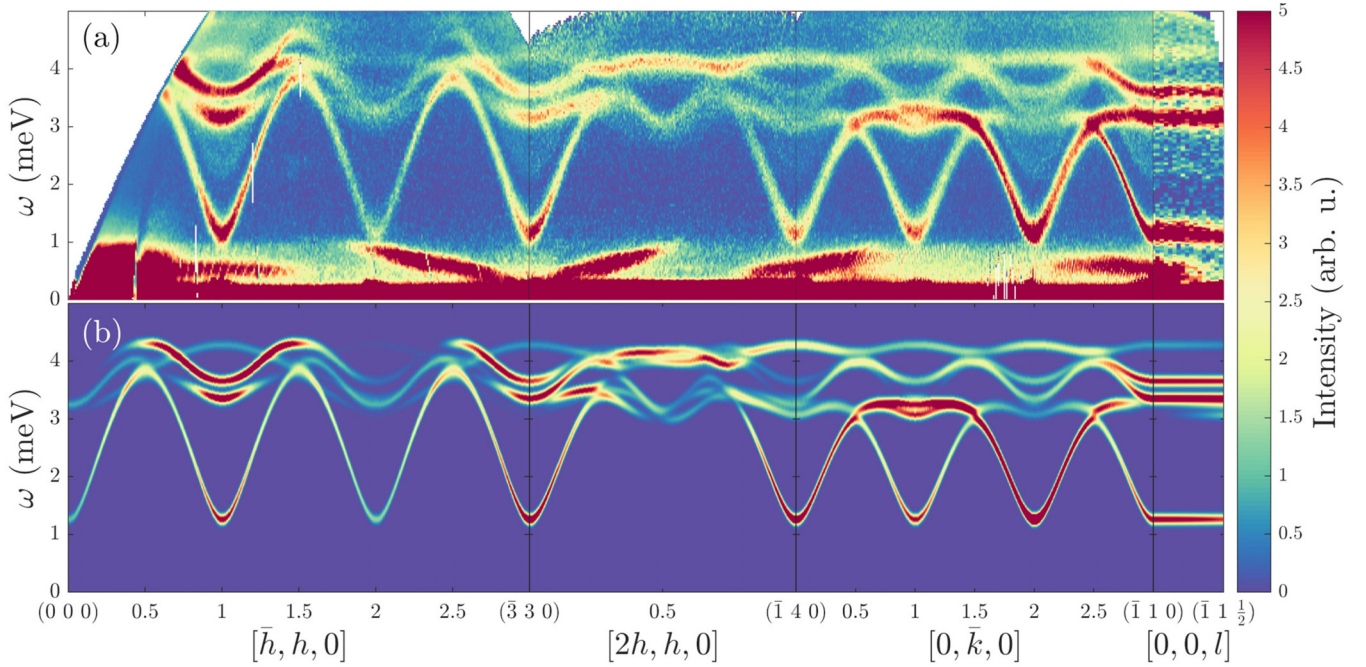


FIG. 5. (a) Dynamical structure factor, $S(\mathbf{Q}, \omega)$, measured on IN5 and shown for the three high-symmetry \mathbf{Q} directions indicated in Fig. 3(g), as well as for the out-of-plane direction. The step size in energy is $dE = 0.04$ meV and in momentum it is $dq = 0.01 \text{ \AA}^{-1}$ in the scattering direction for \mathbf{Q} in the $(hk0)$ plane and $dq = 0.03 \text{ \AA}^{-1}$ for \mathbf{Q} in the $[0, 0, l]$ direction. The integration range in the orthogonal direction is $\pm 0.06 \text{ \AA}^{-1}$. No smoothing effects were introduced to present these data. (b) $S(\mathbf{Q}, \omega)$ modeled using a spin-wave description of the dispersion convolved with Gaussian functions representing the spectrometer resolution.

B. Vertical magnetic field

We turn now to the evolution of the spin excitation spectrum of $\text{Ba}(\text{TiO})\text{Cu}_4(\text{PO}_4)_4$ in the presence of an applied magnetic field. The field adds a term

$$\hat{\mathcal{H}}_m = -g\mu_B \sum_i \mathbf{B} \cdot \mathbf{S}_i \quad (2)$$

to the Hamiltonian of Eq. (1), where the g -factor is assumed to be isotropic, and μ_B is the Bohr magneton. The sample was aligned on IN12 such that the field was applied along the c axis, i.e., $\mathbf{B} = (0, 0, B_z)$. The vertical magnetic field provides significant insight not only into the degeneracy of the $B = 0$ magnetic excitations, which in general should split in the presence of B_z , but also into the effects of the DM interaction, because $[\hat{\mathcal{H}}_m, \hat{\mathcal{H}}_D] \neq 0$, where $\hat{\mathcal{H}}_D$ is the second term of Eq. (1), in any situation other than $\mathbf{D}_{ij} = D_z$ ($\theta = 90^\circ$).

Although one may anticipate from the size of the gap and band center (Sec. IV A) that small fields have little effect on the excitation spectrum, the instrumental resolution of IN12 allowed us to distinguish the split modes even at 1 T. Figure 6 shows the measured scattering intensities, represented as energy scans at a constant $\mathbf{Q} = (1\ 1\ 0)$, for fields of 0, 1, 2, 3, and 5 T. The three sharp modes of the zero-field spectrum shift and split progressively, until at 5 T we observe six well-resolved peaks, all of which are well described by Gaussian profiles. The lowest mode splits clearly into two branches, of equal scattering intensity, which move symmetrically down and up in energy with increasing field. By contrast, the energies and intensities of the two modes in

the high-energy regime show a more complex evolution, on which we comment below.

The spectra of Fig. 6 contain two additional features. One is a broad hump of scattering intensity above 4 meV, which appears to move upwards with field until at 5 T it is centered at 4.5 meV. The other is a broad and weak excitation around 2.1 meV, which we identified previously as a continuum of two-magnon scattering processes. This feature does not move as the field is increased, which is consistent with processes creating two spin waves of $\Delta S^z = 1$ and -1 , such that the composite $\Delta S_{\text{tot}}^z = 0$ excitation does not respond to an external magnetic field.

The field-induced evolution of the spin-wave branches fitted by Gaussians in Fig. 6 is represented as a color map in Fig. 7(a). The low-energy mode and particularly the broad peak above 4 meV show a near-ideal linear splitting from very low fields, whereas the peaks in the 3–3.6 meV regime at $B = 0$ remain rather flat for $B \lesssim 0.5$ T before recovering the same gradient beyond 1.5 T. This indicates differing degrees of sensitivity to the in-plane (noncommuting) component of the DM interaction, although we note that the complex geometry of these interactions on each plaquette [Fig. 1(c)] makes it difficult to equate the field scale with D . The gradients of the linear (Zeeman) evolution beyond 2 T match for all of the split branches observed, with the peak centers of the lowest mode, moving by $-0.09(3)$ and $0.10(3)$ meV/T. These slopes are consistent with the value $g\mu_B = 0.12$ meV/T expected for a spin-1 excitation. The field-induced behavior shown in Fig. 7(a) allows us to deduce the origin of the peaks in the intermediate-energy regime. Of the two peaks apparent at $B = 0$, the one around 3 meV in fact contains three branches,

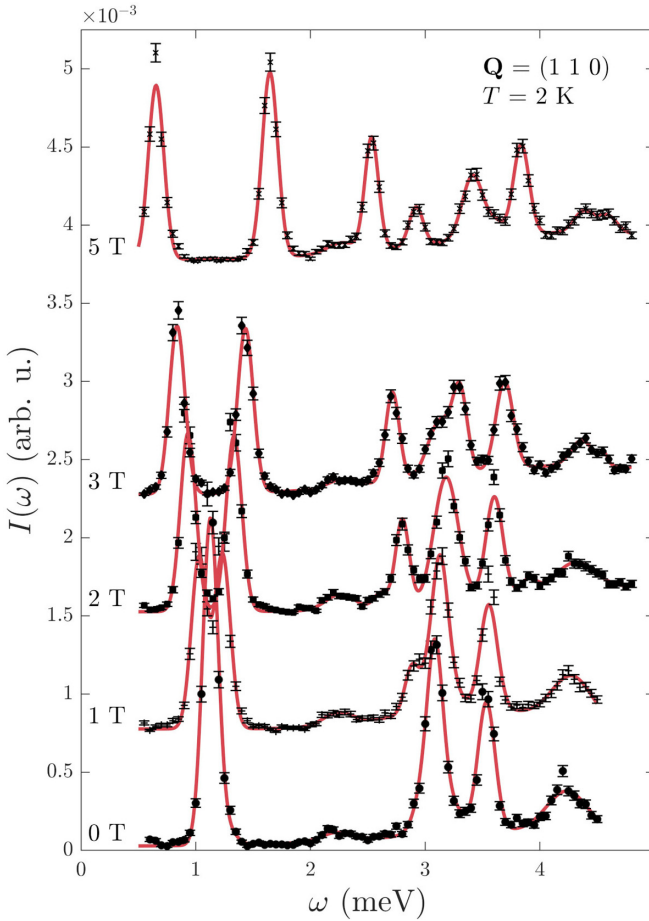


FIG. 6. $I(\mathbf{Q}, \omega)$ measured on IN12 at $\mathbf{Q} = (1\ 1\ 0)$ in vertical magnetic fields of 0, 1, 2, 3, and 5 T. Black points denote measured intensities, normalized by monitor counts, and red lines are obtained from a fit to multiple Gaussian functions.

while the one at 3.5 meV is a single branch. These modes are not degenerate at $B = 0$ because of the DM interaction, which generates the 0.5 meV separation of the $\Delta S^z = \pm 1$ branches.

We have extracted the dynamical structure factor at 5 T from several ω -scans, of the type shown in Fig. 6, measured at multiple \mathbf{Q} points, and in Fig. 7(b) we show the excitation spectrum over half of the BZ in the $[1, k, 0]$ direction. These results verify that each set of split modes disperses in the same way with \mathbf{Q} , i.e., that the effects of the field are the same on each branch at each \mathbf{Q} . No additional splittings are observed with \mathbf{Q} , indicating that $\mathbf{Q} = (1\ 1\ 0)$ has no special symmetries. The different branches disperse differently and we comment that at 5 T they simply cross, showing no evidence of the avoided crossings associated with level mixing.

C. Magnetic Hamiltonian

We now propose a set of parameters that, when inserted in the spin Hamiltonian of Eq. (1), describes the dynamical structure factor of the system both in dispersion and in intensity. In a material with the structure of $\text{Ba}(\text{TiO})\text{Cu}_4(\text{PO}_4)_4$ [Fig. 1(c)], there are *a priori* two separate possibilities for opening the observed gap: the tetramerization and the DM

interaction. Motivated by the relatively large bandwidth of the low-energy excitation [Fig. 5(a)] and the interaction parameters estimated from static measurements [38], we adopt the hypothesis that the system is not strongly tetramerized and the gap arises primarily from the DM term. In addition, the robust ordered moment of $\text{Ba}(\text{TiO})\text{Cu}_4(\text{PO}_4)_4$ suggests that a linear spin-wave (LSW) theory should provide a good approximation in which to describe the magnetic order and excitations, and thus we employ the SPINW package [54].

We obtain a near-optimal set of the parameters specified in Eq. (1) by fitting the measured dispersions throughout the BZ at zero field [Fig. 5(a)], with additional information taken from the available finite-field dispersions (Fig. 7). The geometry of these interactions is shown in Fig. 1(c) and their values are given in Table I. We stress that we have not performed a global minimization in the entire parameter space, and that the parameters we identify therefore constitute an informed and highly accurate local minimum. A quantitative estimate of the uncertainties on the strongly interdependent Heisenberg parameters is difficult to extract from SPINW, and instead we alter each parameter individually to establish the limits of the local minimum; these are a direct reflection of the physics of the system, as discussed below, and one clear example is that the uncertainty in $D = 1.07(3)$ meV is established quite directly by the measured spin gap. The ordered ground state corresponding to these parameters is qualitatively similar to that deduced from SNP measurements [43] and shown in Fig. 2, with the Cu spins forming a canted two-in, two-out arrangement on each cupola. However, the spin direction in the zero-field ground state estimated in the SNP analysis is almost normal to the CuO_4 squares, making an angle of 45° with the (ab) plane, whereas for the ground state deduced from the LSW description this angle is 63° . We return to this issue after discussing the relative values of D and the Heisenberg parameters $\{J_m\}$.

The zero-field excitation spectrum produced with the model parameters of Table I is shown in Fig. 5(b). It is clear that all the primary features of the measured bands are captured with quantitative accuracy. Crucial confirmation of this parameter set is provided by the fact that the scattered intensities are very well reproduced with no further fitting. The level of the remaining discrepancies is extremely small, and concerns mostly details of apparent (anti)crossing events between rather flat modes in the high-energy regime, although some of these may be a consequence only of low intensities. We note that the feature $E_{2M}(\mathbf{Q})$ with onset around 2.1 meV is not present in the fitted spectrum, consistent with our conclusion that it is not an elementary spin wave but a two-magnon scattering state. Concerning the field-induced evolution of these modes, again the fits (dotted lines) in Fig. 7(a) show

TABLE I. Interaction parameters, in meV, used in the LSW description of the magnetic spectrum of Figs. 5(a) and 7(b). The geometry of these interactions is shown in Fig. 1(c), and the meaning of the angle θ is given in Fig. 2(b).

J_1	J_2	J'_2	J'_{11}	J'_{12}	D	θ
2.03(6)	0.52(5)	2.22(6)	0.17(3)	0.17(3)	1.07(3)	$10(3)^\circ$

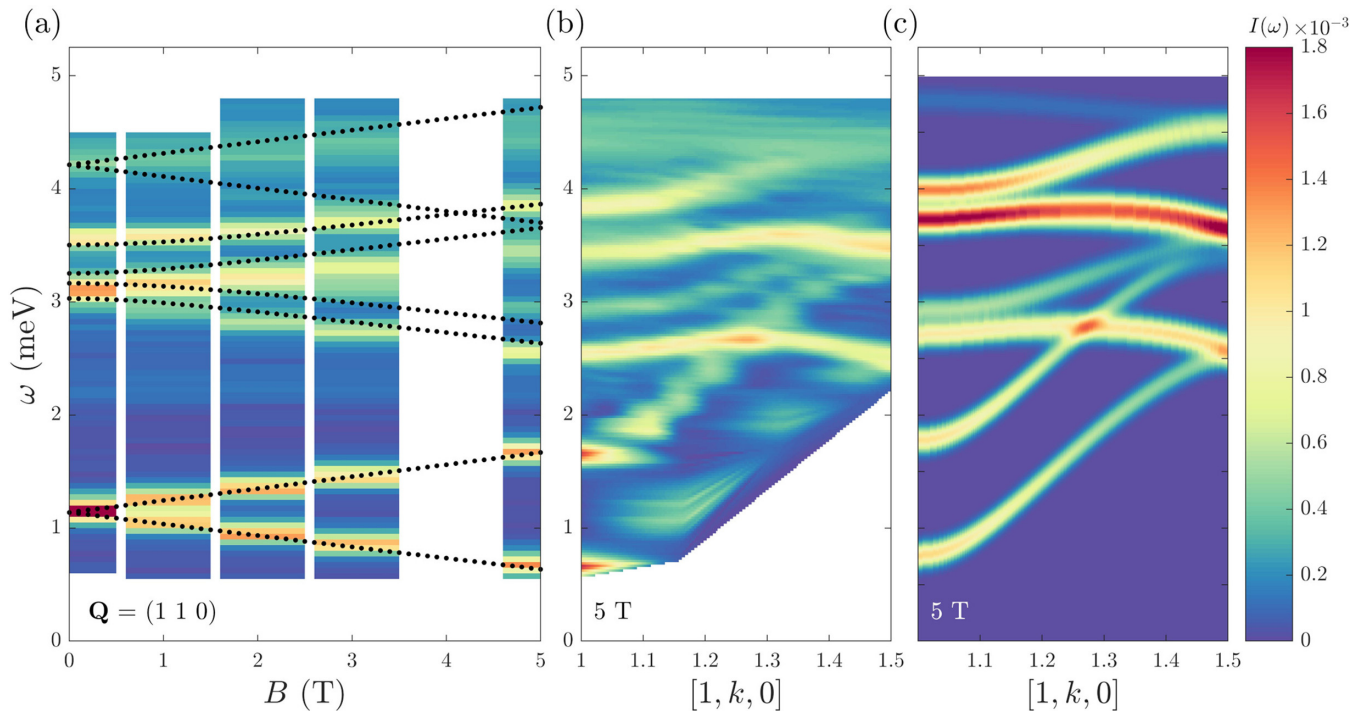


FIG. 7. (a) Intensity data of Fig. 6 presented as a color map for the five measured magnetic field values. Black points show the energies of the magnetic excitations at $\mathbf{Q} = (1\ 1\ 0)$ obtained from LSW calculations based on the Hamiltonian of Eq. (2) with the parameters of Table I. (b) Excitation spectrum measured on IN12 at 5 T along the $[1, k, 0]$ direction. For a better representation of these data, a linear interpolation was applied to measurements at discrete \mathbf{Q} points of the type shown in Fig. 6. (c) Excitation spectrum in a field of 5 T, modeled in the LSW approximation for this half-BZ \mathbf{Q} -scan.

only very minor deviations from the measured data for only one of the multiplets at intermediate energies.

The Heisenberg interactions of Table I define a magnetic lattice of square antiferromagnetic plaquettes, J_1 , with a small diagonal intraplaquette coupling, J_2 , generating rather weak frustration. While J_1 is determined rather accurately by the measured band center, J_2 has little direct influence on the spectrum and hence a relatively larger uncertainty (Table I). The dominant interaction linking the plaquettes in the ab plane is not J'_1 , the bond that would form a conventional square lattice, but the diagonal coupling, J'_2 . This result is consistent with the geometry of the Cu–O–P–O–Cu bonds connecting the plaquettes, which, as represented in Fig. 1(b), almost form a single curve for J'_2 but include an additional 90° kink for J'_1 . The magnitude of J'_2 can be fitted to high accuracy from the dispersion of the lowest mode, and one of our most striking results is that the optimal J'_2 is slightly (10%) larger than J_1 (whose Cu–O–Cu bond angle is only 108°). This implies that the degree of tetramerization contained within the Heisenberg parameters alone is rather small. It also indicates that the interplaquette coupling is twice as strong as the value proposed in Ref. [38], and in Sec. V we investigate this discrepancy. Finally, the structure of $\text{Ba}(\text{TiO})\text{Cu}_4(\text{PO}_4)_4$ requires two different J'_1 bonds, which we label J'_{11} and J'_{12} , and we find these to be similar in value but weak by comparison with J'_2 (Table I). In the spin-wave spectrum of Fig. 5, these interactions are necessary for an accurate description of the separation between closely spaced modes in the high-energy regime, particularly around 3 meV, and our fitting quality deteriorates when they are not equal and antiferromagnetic.

By contrast, these two parameters were given opposite signs in fitting the magnetization data, suggesting that smaller parameters in the global fit can be subject to large relative uncertainties.

The other strong interaction in Table I is the DM term, whose vector nature results in two unknown parameters, equivalently (D, θ) or the projections $D_{\parallel} = D \cos \theta = 1.05(3)$ meV in the ab plane (orthogonal to the J_1 bond) and $D_z = D \sin \theta = 0.18$ meV along the c axis. By symmetry, the vector \mathbf{D} lies in the plane orthogonal to the Cu–Cu bond of J_1 and its direction alternates between all-in or all-out [Fig. 1(c)] with the upward or downward cupola orientation. The strong J'_2 interaction means that the origin of the gap must lie in the DM term, and thus it is no surprise to find a large magnitude, D . In more detail, the fitted gap is extremely sensitive to the value of D_{\parallel} , fixing its value within a narrow window, whereas any value of D_z below 0.8 meV has rather little effect.

For a more accurate determination of the direction, θ , of the DM vector, we exploit the fact that its in- and out-of-plane components have quite different effects on the $\text{SU}(2)$ -symmetric eigenstates of the Heisenberg terms in $\hat{\mathcal{H}}$ [Eq. (1)] and on the Zeeman-split eigenstates in the presence of $\hat{\mathcal{H}}_m$ [Eq. (2)]. In zero field it is easy to demonstrate that the parameters of Table I provide a consistent description of certain mode separations in the high-energy regime, which cannot be achieved using the interplaquette J_m parameters alone, but it is difficult to demonstrate uniqueness. By contrast, the finite-field data we show in Fig. 7(a) provide detailed information about field gradients and anticrossings that are reproduced accurately (black dotted lines). The 5 T dispersion

and intensity data of Fig. 7(b) are also fitted with quantitative accuracy by the LSW description with these \mathbf{D} parameters, as shown in Fig. 7(c). These LSW calculations also indicate that D_z values in excess of 0.18 meV cause a visible splitting of the 2.5 meV mode in Fig. 7(c), which sets an upper limit on this quantity.

The resulting value, $\theta = 10^\circ$, is in complete agreement with the conclusions drawn from static measurements [38]. On structural grounds, one might expect this angle to take the value $\theta_p = 14^\circ$ obtained for a single cupola bond from $\mathbf{D}_{ij} \propto \mathbf{r}_i \times \mathbf{r}_j$ [Fig. 2(b)]. Thus both static and dynamic measurements indicate only minimal corrections to this expectation, despite the potentially complex spin-density distribution in the full cupola wave function. Returning to the spin orientation in the ground state, the LSW result that the ordered moments on the square are canted at 27° from the c axis translates to an angle of 37° between the two antialigned spins on a bond. Given the relative strengths of the leading J terms, which favor collinear order, and the DM term, which favors a 90° angle, the value of 37° is fully consistent.

As noted in Sec. I, the greater data volume provided by the dynamical excitations and their higher sensitivity to the coupling parameters of the system allows us to obtain a more accurate account of the magnetic interactions than was possible using static measurements. The primary point of difference with the previous results [37,38] is the much larger interplaquette coupling provided by J'_2 . Next we provide (Sec. V) a more detailed discussion of the implications of this result for fitting the high-field magnetization data and for understanding the further properties of the system, including magnetoelectricity.

Before turning to this issue, we close our discussion of parameters by noting that a weak interlayer interaction, J_\perp , is required to ensure the observed antiferromagnetic order. In principle, this parameter could be fitted from the very weakly dispersive behavior of the low-energy mode for wave vectors \mathbf{Q} in the $[0, 0, l]$ direction (Fig. 5). In the present experiment, geometrical and resolution factors were such that our data for the out-of-plane direction are of qualitative value only, and thus we did not attempt to include J_\perp in our fitting procedure. All of our observations are consistent with the order-of-magnitude estimate $J_\perp \approx J_1/100$ proposed in previous studies [38]. The resulting strongly 2D nature of the $A(BO)Cu_4(PO_4)_4$ family of compounds, combined with the clearly resolvable effects of all the different parameters in Table I, makes them valuable candidates for investigating quantum phases in spatially and spin-anisotropic square-lattice models, as we discuss further in Sec. VI.

V. HIGH-FIELD MAGNETIZATION

The INS interaction parameters we obtain have direct implications for all of the magnetic, and by extension magnetoelectric, properties of $Ba(TiO)Cu_4(PO_4)_4$. The most detailed thermodynamic data available take the form of high-field magnetization measurements, which were performed in Ref. [38] up to full saturation at fields in excess of 60 T. We repeat the CMF analysis of these data [38] using the parameters deduced from INS, and the results are shown in Figs. 8(a) and 8(b).

The magnetization measurements of Ref. [38], reproduced in Figs. 8(c) and 8(d), are described to semiquantitative accuracy by CMF modeling with the parameters of Table I. This degree of consistency is eminently reassuring, and it establishes the relative values of the INS parameters as the updated benchmark for $Ba(TiO)Cu_4(PO_4)_4$. However, given that the magnetization data were modeled previously with a much smaller J'_2 , the question remains as to whether any given set of proposed parameters can be established uniquely. Here it is important to note that the two methods of analysis are quite different, as the CMF approach is based around the limit of weakly coupled plaquettes, whereas LSW theory is based on the assumption of robust magnetic order throughout the system (meaning strongly coupled plaquettes). While a direct comparison is therefore not necessarily meaningful, our results provide an example in which their predictions agree rather well; LSW theory is justified by the strong J'_2 , and the CMF method remains within its range of applicability because the net intraplaquette interactions, $J_1 + D$ per bond, still exceed the interplaquette J'_2 .

Qualitatively, this degree of consistency between the LSW and CMF descriptions of the magnetization suggests that there are no major discrepancies over issues such as the moment direction and the orientation or magnitude of the DM vector. The CMF results show two magnetic phases below saturation, as deduced from the strongly anisotropic response to fields applied in different crystallographic directions (Fig. 8). In addition to these phases I and II, it was suggested [38] that the system may be close to a predicted phase III. However, no evidence for this possibility appears in purely magnetic measurements, and thus more sensitive dielectric measurements are required for a deeper analysis. One may also consider different materials in the family of $A(BO)Cu_4(PO_4)_4$ compounds for a broader investigation of possible magnetic phases in this complex geometry.

Quantitatively, the INS parameters appear to overestimate the experimental saturation fields (57–63 T for different field directions) by approximately 20% (Fig. 8). The saturation field is in general a coordination-weighted sum of all the J_m parameters in Table I. We note that in a pure Heisenberg model on the 2D square lattice, the LSW approximation has been shown theoretically [55] to overestimate the values of J_m by a factor $Z_c = 1.18$, as a consequence of the fact that it does not include quantum fluctuation corrections. The applicability of Z_c has been verified in experiment [30], and in Figs. 8(c) and 8(d) we show a revised fit in which the J_m values have been renormalized downwards by a factor of Z_c , demonstrating that this correction alone is sufficient to achieve a quantitative match between our static and dynamic measurements.

VI. DISCUSSION

The two key features of the parameter set we identify that defines the magnetic lattice in $Ba(TiO)Cu_4(PO_4)_4$ (Table I) are the strength of the diagonal interplaquette coupling ($J'_2 \approx J_1$) and the strong intraplaquette DM interaction ($D \approx J_1/2$). As noted in Sec. I, the isotropic (Heisenberg) tetramerized J_1 - J'_1 model has a quantum phase transition from a gapless magnetically ordered phase to a gapped plaquette-singlet phase at $\alpha_c = J'_1/J_1 \approx 0.55$ [18,19]. At lowest order,

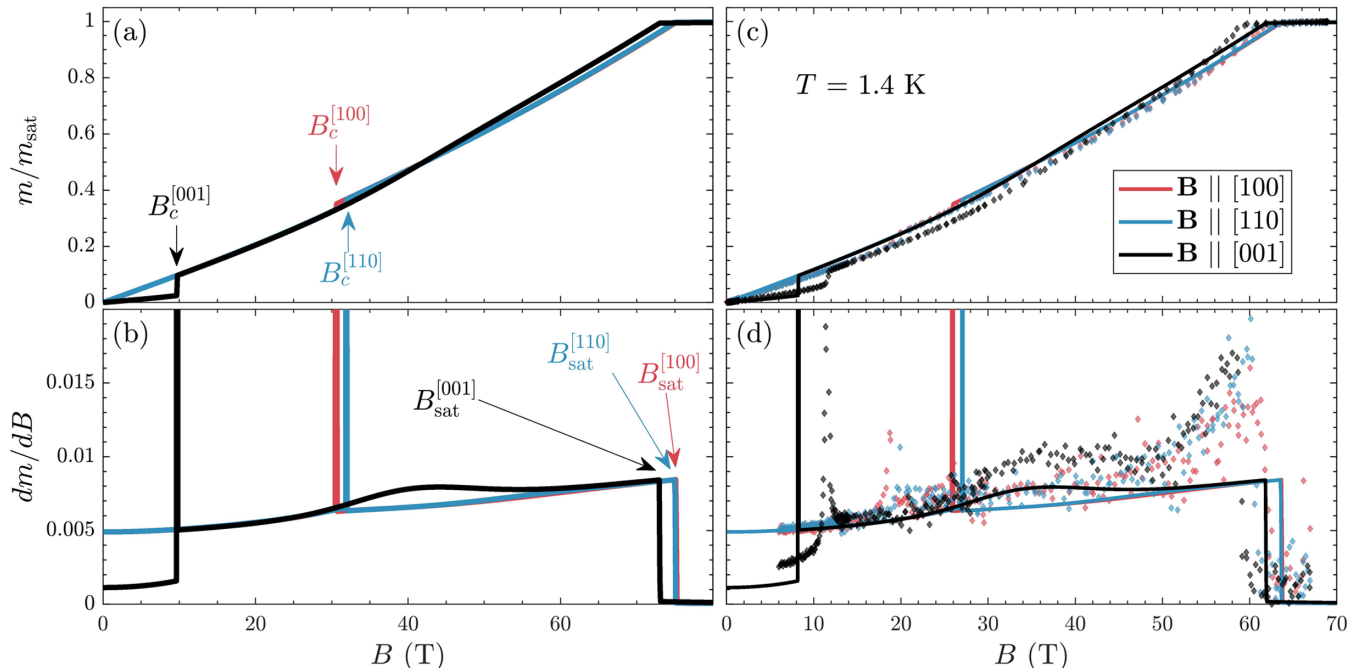


FIG. 8. (a) Magnetization, $m(B)$, calculated using the magnetic interaction parameters of Table I, for fields applied in the three primary crystallographic directions of the tetragonal structure (Fig. 1). m_{sat} denotes the saturation magnetization and is used for normalization. (b) Calculated magnetization derivative, $dm(B)/dB$, which highlights the discontinuous features in $m(B)$. (c) Normalized magnetization measurements of Ref. [38]. (d) Measured magnetization derivative. The features at the different fields B_c , where the gap is closed, and B_{sat} , where saturation is achieved, demarcate two distinct magnetic phases. The solid lines in panels (c) and (d) show that quantitative agreement with experiment is obtained if the interaction parameters are scaled downwards by the factor $Z_c = 1.18$ arising from the corrections to LSW theory [55].

the J_1 - J'_2 model defined by the leading Heisenberg terms in $\text{Ba}(\text{TiO})\text{Cu}_4(\text{PO}_4)_4$ would have the same behavior, with an inverted ordering pattern between plaquettes, in which case the J'_2/J_1 ratio would place the system well in the ordered phase. While further efforts have been applied to understanding the disordered phases arising in tetramerized square-lattice models [13,56,57], no anisotropy has yet been considered.

In systems with DM interactions only on the interplaquette bonds, a gap is always present but a critical point remains, with α_c being determined from the onset of an ordered moment, and this type of physics has been discussed for the square-lattice dimer system $\text{Sr}_3\text{Ir}_2\text{O}_7$ [58]. However, intraplaquette DM interactions cause an admixture of triplets and quintuplets into the ground state at any finite D , as has been shown for coupled tetrahedra in the pyrochlore geometry [25]. The generic situation in a square-lattice model is then the immediate onset of long-range order in addition to the opening of a magnon gap, and as a result the $A(\text{BO})\text{Cu}_4(\text{PO}_4)_4$ family of compounds is pushed away from the phase space of gapped tetramerized $S = 1/2$ systems.

For the geometry of $\text{Ba}(\text{TiO})\text{Cu}_4(\text{PO}_4)_4$, the intraplaquette spin configuration is that shown in Fig. 2(a), which is controlled by D_{\parallel} rather than by D_z (Table I). The interplaquette alignment of cupola units presents no frustration problem when comparing J'_1 with J'_2 interactions, because the DM terms remain satisfied for either relative alignment of the S_z spin components [Fig. 1(c)]. Even in a system with very weak interplaquette coupling, the action of the intraplaquette DM terms remains that of inducing a weak ordered moment, whose fluctuations are gapped magnon excitations, and these

features are superposed upon the quantum fluctuation effects favoring isolated plaquette states. A heuristic measure of the influence of the strong DM interactions in $\text{Ba}(\text{TiO})\text{Cu}_4(\text{PO}_4)_4$ on suppressing these quantum fluctuation effects can be obtained from the ordered moment, which was estimated from a detailed analysis of the magnetic structure at 80% of the maximal value [43], as opposed to 61% in an isotropic square lattice [6].

Although the strong interplaquette interactions in $\text{Ba}(\text{TiO})\text{Cu}_4(\text{PO}_4)_4$ place it rather far from the parameter regime for investigating weak magnetic order coexisting with strong quantum fluctuations, they do make this material an excellent candidate for the study of topological magnon states [59–61]. It has been shown for both topological magnon [61,62] and triplon systems [63] that the combination of multiple DM terms with an external magnetic field [62,63] leads to symmetry-preserved topological modes that exhibit Dirac-cone level crossing rather than level repulsion and anticrossing. We observe from Fig. 6 that a field-driven gap closure, which is a candidate topological quantum phase transition, can be expected in $\text{Ba}(\text{TiO})\text{Cu}_4(\text{PO}_4)_4$ at approximately 12 T (Fig. 8) [38].

VII. SUMMARY

We have measured the spin dynamics of the compound $\text{Ba}(\text{TiO})\text{Cu}_4(\text{PO}_4)_4$, which is composed of Cu_4O_{12} “cupola” units coupled into 2D square-lattice planes. Our high-quality data reveal a complex spectrum of well-resolved magnetic excitations, whose evolution and systematic splitting we have

followed to an applied magnetic field of 5 T. Despite the presence of robust magnetic order, the lowest-lying spin excitation has a large gap, of half its bandwidth, indicating the presence of significant DM interactions. We obtain a quantitatively accurate description of every aspect of the measured spectrum by using a linear spin-wave theory, which indicates the primacy of the ordered moment in determining the appropriate description of the magnetic properties. Our fitted spectra indicate that the four-site plaquette units have strong intraplaquette DM interactions (D) and strong interplaquette Heisenberg coupling (J'_2). The values we obtain, $D \simeq 0.53J_1$ and $J'_2 \simeq 1.09J_1$, give results fully consistent with static measurements up to very high applied fields and thus set the benchmark for $\text{Ba}(\text{TiO})\text{Cu}_4(\text{PO}_4)_4$. Although the minimal tetramerization and strong intraplaquette DM interactions in the $A(\text{BO})\text{Cu}_4(\text{PO}_4)_4$ compounds suppress quantum fluctuation effects in favor of noncoplanar magnetic order, they also give this family of materials high potential for the systematic study of topological magnetic states and topological magnon excitations.

ACKNOWLEDGMENTS

We thank F. Groitl, F. Mila, and G. S. Tucker for helpful discussions. We are grateful to the Swiss National Science Foundation (SNSF) for financial support under Grant No. 188648, to the European Research Council (ERC) for the support of the Synergy network HERO (Grant No. 810451), to the Japan Society for the Promotion of Science (JSPS) for the support of KAKENHI Grants No. JP19H05823 and No. JP19H01847, and for the support of the Japanese MEXT Leading Initiative for Excellent Young Researchers (LEADER). Access to MACS was provided by the Center for High Resolution Neutron Scattering, a partnership between the National Institute of Standards and Technology and the National Science Foundation under Agreement No. DMR-1508249. Data collected at the Institut Laue-Langevin in the course of this study are available in Refs. [50,51]. The work performed on IN12 was supported by the Swiss State Secretariat for Education, Research, and Innovation (SERI) through a CRG Grant.

-
- [1] H. Bethe, Zur theorie der metalle, *Z. Phys.* **71**, 205 (1931).
- [2] L. D. Faddeev and L. A. Takhtajan, What is the spin of a spin wave? *Phys. Lett. A* **85**, 375 (1981).
- [3] G. Müller, H. Thomas, H. Beck, and J. C. Bonner, Quantum spin dynamics of the antiferromagnetic linear chain in zero and nonzero magnetic field, *Phys. Rev. B* **24**, 1429 (1981).
- [4] L. Néel, Propriétés magnétiques des ferrites; Ferrimagnétisme et antiferromagnétisme, *Ann. Phys.* **12**, 137 (1948).
- [5] C. G. Shull, W. A. Strauser, and E. O. Wollan, Neutron diffraction by paramagnetic and antiferromagnetic substances, *Phys. Rev.* **83**, 333 (1951).
- [6] E. Manousakis, The spin- $\frac{1}{2}$ Heisenberg antiferromagnet on a square lattice and its application to the cuprous oxides, *Rev. Mod. Phys.* **63**, 1 (1991).
- [7] P. Anderson, Resonating valence bonds: A new kind of insulator? *Mater. Res. Bull.* **8**, 153 (1973).
- [8] P. A. Lee, N. Nagaosa, and X.-G. Wen, Doping a Mott insulator: Physics of high-temperature superconductivity, *Rev. Mod. Phys.* **78**, 17 (2006).
- [9] P. Chandra and B. Douçot, Possible spin-liquid state at large S for the frustrated square Heisenberg lattice, *Phys. Rev. B* **38**, 9335 (1988).
- [10] L. Balents, Spin liquids in frustrated magnets, *Nature (London)* **464**, 199 (2010).
- [11] L. Isaev, G. Ortiz, and J. Dukelsky, Hierarchical mean-field approach to the $J_1 - J_2$ Heisenberg model on a square lattice, *Phys. Rev. B* **79**, 024409 (2009).
- [12] O. Götze, S. E. Krüger, F. Fleck, J. Schulenburg, and J. Richter, Ground-state phase diagram of the spin- $\frac{1}{2}$ square-lattice $J_1 - J_2$ model with plaquette structure, *Phys. Rev. B* **85**, 224424 (2012).
- [13] R. L. Doretto, Plaquette valence-bond solid in the square-lattice $J_1 - J_2$ antiferromagnet Heisenberg model: A bond operator approach, *Phys. Rev. B* **89**, 104415 (2014).
- [14] S.-S. Gong, W. Zhu, D. N. Sheng, O. I. Motrunich, and M. P. A. Fisher, Plaquette Ordered Phase and Quantum Phase Diagram in the Spin- $\frac{1}{2}$ $J_1 - J_2$ Square Heisenberg Model, *Phys. Rev. Lett.* **113**, 027201 (2014).
- [15] S. Morita, R. Kaneko, and M. Imada, Quantum spin liquid in spin $\frac{1}{2}$ $J_1 - J_2$ Heisenberg model on square lattice: Many-variable variational Monte Carlo study combined with quantum-number projections, *J. Phys. Soc. Jpn.* **84**, 024720 (2015).
- [16] L. Wang and A. W. Sandvik, Critical Level Crossings and Gapless Spin Liquid in the Square-Lattice Spin-1/2 $J_1 - J_2$ Heisenberg Antiferromagnet, *Phys. Rev. Lett.* **121**, 107202 (2018).
- [17] R. Haghshenas and D. N. Sheng, $U(1)$ -symmetric infinite projected entangled-pair states study of the spin-1/2 square $J_1 - J_2$ Heisenberg model, *Phys. Rev. B* **97**, 174408 (2018).
- [18] A. F. Albuquerque, M. Troyer, and J. Oitmaa, Quantum phase transition in a Heisenberg antiferromagnet on a square lattice with strong plaquette interactions, *Phys. Rev. B* **78**, 132402 (2008).
- [19] S. Wenzel, L. Bogacz, and W. Janke, Evidence for an Unconventional Universality Class from a Two-Dimensional Dimerized Quantum Heisenberg Model, *Phys. Rev. Lett.* **101**, 127202 (2008).
- [20] R. F. Bishop, P. H. Y. Li, D. J. J. Farnell, J. Richter, and C. E. Campbell, Frustrated Heisenberg antiferromagnet on the checkerboard lattice: $J_1 - J_2$ model, *Phys. Rev. B* **85**, 205122 (2012).
- [21] Y. Xu, Z. Xiong, H.-Q. Wu, and D.-X. Yao, Spin excitation spectra of the two-dimensional $S = \frac{1}{2}$ Heisenberg model with a checkerboard structure, *Phys. Rev. B* **99**, 085112 (2019).
- [22] I. Dzyaloshinsky, A thermodynamic theory of "weak" ferromagnetism of antiferromagnetics, *J. Phys. Chem. Solids* **4**, 241 (1958).
- [23] T. Moriya, Anisotropic Superexchange Interaction and Weak Ferromagnetism, *Phys. Rev.* **120**, 91 (1960).
- [24] S. Miyahara, J.-B. Fouet, S. R. Manmana, R. M. Noack, H. Mayaffre, I. Sheikin, C. Berthier, and F. Mila, Uniform and staggered magnetizations induced by Dzyaloshinskii-Moriya interactions in isolated and coupled spin-1/2 dimers in a magnetic field, *Phys. Rev. B* **75**, 184402 (2007).

- [25] V. N. Kotov, M. E. Zhitomirsky, M. Elhajal, and F. Mila, Weak antiferromagnetism and dimer order in quantum systems of coupled tetrahedra, *Phys. Rev. B* **70**, 214401 (2004).
- [26] B. Xi, S. Hu, J. Zhao, G. Su, B. Normand, and X. Wang, Low-energy properties of anisotropic two-dimensional spin- $\frac{1}{2}$ Heisenberg models in staggered magnetic fields, *Phys. Rev. B* **84**, 134407 (2011).
- [27] S. Rufo, J. R. de Sousa, and J. A. Plascak, Exchange frustration effect due to anisotropies on the spin- $1/2$ $J_1 - J'_1 - J_2$, *Physica A* **518**, 349 (2019).
- [28] R. Coldea, S. M. Hayden, G. Aeppli, T. G. Perring, C. D. Frost, T. E. Mason, S.-W. Cheong, and Z. Fisk, Spin Waves and Electronic Interactions in La_2CuO_4 , *Phys. Rev. Lett.* **86**, 5377 (2001).
- [29] N. S. Headings, S. M. Hayden, R. Coldea, and T. G. Perring, Anomalous High-Energy Spin Excitations in the High- T_c Superconductor-Parent Antiferromagnet La_2CuO_4 , *Phys. Rev. Lett.* **105**, 247001 (2010).
- [30] H. M. Rønnow, D. F. McMorrow, R. Coldea, A. Harrison, I. D. Youngson, T. G. Perring, G. Aeppli, O. Syljuåsen, K. Lefmann, and C. Rischel, Spin Dynamics of the 2D Spin $\frac{1}{2}$ Quantum Antiferromagnet Copper Deuterioformate Tetradeuterate (CFTD), *Phys. Rev. Lett.* **87**, 037202 (2001).
- [31] P. Babkevich, V. M. Katukuri, B. Fåk, S. Rols, T. Fennell, D. Pajić, H. Tanaka, T. Pardini, R. R. P. Singh, A. Mitrushchenkov, O. V. Yazyev, and H. M. Rønnow, Magnetic Excitations and Electronic Interactions in $\text{Sr}_2\text{CuTeO}_6$: A Spin- $\frac{1}{2}$ Square Lattice Heisenberg Antiferromagnet, *Phys. Rev. Lett.* **117**, 237203 (2016).
- [32] A. A. Tsirlin and H. Rosner, Extension of the spin- $\frac{1}{2}$ frustrated square lattice model: The case of layered vanadium phosphates, *Phys. Rev. B* **79**, 214417 (2009).
- [33] A. A. Tsirlin, R. Nath, A. M. Abakumov, Y. Furukawa, D. C. Johnston, M. Hemmida, H.-A. Krug von Nidda, A. Loidl, C. Geibel, and H. Rosner, Phase separation and frustrated square lattice magnetism of $\text{Na}_{1.5}\text{VOPO}_4\text{F}_{0.5}$, *Phys. Rev. B* **84**, 014429 (2011).
- [34] J.-X. Zhu, R. Yu, H. Wang, L. L. Zhao, M. D. Jones, J. Dai, E. Abrahams, E. Morosan, M. Fang, and Q. Si, Band Narrowing and Mott Localization in Iron Oxychalcogenides $\text{La}_2\text{O}_2\text{Fe}_2\text{O}(\text{Se}, \text{S})_2$, *Phys. Rev. Lett.* **104**, 216405 (2010).
- [35] K. Kimura, M. Sera, and T. Kimura, A^{2+} Cation Control of Chiral Domain Formation in $A(\text{TiO})\text{Cu}_4(\text{PO}_4)_4$ ($A = \text{Ba}, \text{Sr}$), *Inorg. Chem.* **55**, 1002 (2016).
- [36] K. Kimura, D. Urushihara, T. Asaka, M. Toyoda, A. Miyake, M. Tokunaga, A. Matsuo, K. Kindo, K. Yamauchi, and T. Kimura, Synthesis, structure, and anomalous magnetic ordering of the spin- $1/2$ coupled square tetramer system $\text{K}(\text{NbO})\text{Cu}_4(\text{PO}_4)_4$, *Inorg. Chem.* **59**, 10986 (2020).
- [37] K. Kimura, P. Babkevich, M. Sera, M. Toyoda, K. Yamauchi, G. S. Tucker, J. Martius, T. Fennell, P. Manuel, D. D. Khalyavin, R. D. Johnson, T. Nakano, Y. Nozue, H. M. Rønnow, and T. Kimura, Magnetodielectric detection of magnetic quadrupole order in $\text{Ba}(\text{TiO})\text{Cu}_4(\text{PO}_4)_4$ with Cu_4O_{12} square cupolas, *Nat. Commun.* **7**, 13039 (2016).
- [38] Y. Kato, K. Kimura, A. Miyake, M. Tokunaga, A. Matsuo, K. Kindo, M. Akaki, M. Hagiwara, M. Sera, T. Kimura, and Y. Motome, Magnetoelectric Behavior from $S = 1/2$ Asymmetric Square Cupolas, *Phys. Rev. Lett.* **118**, 107601 (2017).
- [39] K. Kimura, M. Toyoda, P. Babkevich, K. Yamauchi, M. Sera, V. Nassif, H. M. Rønnow, and T. Kimura, A-cation control of magnetoelectric quadrupole order in $A(\text{TiO})\text{Cu}_4(\text{PO}_4)_4$ ($A = \text{Ba}, \text{Sr}$, and Pb), *Phys. Rev. B* **97**, 134418 (2018).
- [40] S. S. Islam, K. M. Ranjith, M. Baenitz, Y. Skourski, A. A. Tsirlin, and R. Nath, Frustration of square cupola in $\text{Sr}(\text{TiO})\text{Cu}_4(\text{PO}_4)_4$, *Phys. Rev. B* **97**, 174432 (2018).
- [41] Y. Kato, K. Kimura, A. Miyake, M. Tokunaga, A. Matsuo, K. Kindo, M. Akaki, M. Hagiwara, S. Kimura, T. Kimura, and Y. Motome, Magnetoelectric behavior from cluster multipoles in square cupolas: Study of $\text{Sr}(\text{TiO})\text{Cu}_4(\text{PO}_4)_4$ in comparison with Ba and Pb isostructurals, *Phys. Rev. B* **99**, 024415 (2019).
- [42] V. Kumar, A. Shahee, S. Kundu, M. Baenitz, and A. V. Mahajan, The spin- $1/2$ coupled tetramer system $\text{Ba}(\text{TiO})\text{Cu}_4(\text{PO}_4)_4$ probed by magnetization, specific heat, and ^{31}P NMR, *J. Magn. Magn. Mater.* **492**, 165600 (2019).
- [43] P. Babkevich, L. Testa, K. Kimura, T. Kimura, G. S. Tucker, B. Roessli, and H. M. Rønnow, Magnetic structure of $\text{Ba}(\text{TiO})\text{Cu}_4(\text{PO}_4)_4$ probed using spherical neutron polarimetry, *Phys. Rev. B* **96**, 214436 (2017).
- [44] K. Kimura, T. Katsuyoshi, Y. Sawada, S. Kimura, and T. Kimura, Imaging switchable magnetoelectric quadrupole domains via nonreciprocal linear dichroism, *Commun. Mater.* **1**, 39 (2020).
- [45] M. Akaki, K. Kimura, Y. Kato, Y. Sawada, Y. Narumi, H. Ohta, T. Kimura, Y. Motome, and M. Hagiwara, Nonreciprocal linear dichroism observed in electron spin resonance spectra of the magnetoelectric multiferroic $\text{Pb}(\text{TiO})\text{Cu}_4(\text{PO}_4)_4$, *Phys. Rev. Research* **3**, L042043 (2021).
- [46] K. Kimura, M. Sera, T. Nakano, Y. Nozue, and T. Kimura, Magnetodielectric properties of the square cupola antiferromagnet $\text{Ba}(\text{TiO})\text{Cu}_4(\text{PO}_4)_4$, *J. Phys. B* **536**, 93 (2018).
- [47] K. Kimura, S. Kimura, and T. Kimura, Magnetoelectric Behaviors in Magnetic-Field-Induced Phases of $\text{Pb}(\text{TiO})\text{Cu}_4(\text{PO}_4)_4$, *J. Phys. Soc. Jpn.* **88**, 093707 (2019).
- [48] R. Råsta, I. Heinmaa, K. Kimura, T. Kimura, and R. Stern, Magnetic structure of the square cupola compound $\text{Ba}(\text{TiO})\text{Cu}_4(\text{PO}_4)_4$, *Phys. Rev. B* **101**, 054417 (2020).
- [49] J. A. Rodriguez, D. M. Adler, P. C. Brand, C. Broholm, J. C. Cook, C. Brocker, R. Hammond, Z. Huang, P. Hundertmark, and J. W. Lynn, MACS—a new high intensity cold neutron spectrometer at NIST, *Meas. Sci. Technol.* **19**, 034023 (2008).
- [50] P. Babkevich, L. Testa, H. M. Rønnow, K. Kimura, and J. Ollivier, *Magnetic Excitation Spectrum in a Chiral Quantum Magnet* (Institut Laue-Langevin, France, 2016).
- [51] L. Testa, H. M. Rønnow, and S. Raymond, *Tracking Magnetic Excitations in $\text{Ba}(\text{TiO})\text{Cu}_4(\text{PO}_4)_4$ with a Vertical Magnet* (Institut Laue-Langevin, France, 2019).
- [52] R. A. Ewings, A. Buts, M. D. Le, J. van Duijn, I. Bustinduy, and T. G. Perring, HORACE: Software for the analysis of data from single crystal spectroscopy experiments at time-of-flight neutron instruments, *Nucl. Instrum. Methods Phys. Res., Sect. A* **834**, 132 (2016).
- [53] R. Juneja, S. Thébaud, T. Pandey, C. Polanco, D. Moseley, M. Manley, Y. Cheng, B. Winn, D. Abernathy, R. Hermann, and L. Lindsay, Quasiparticle twist dynamics in non-symmorphic materials, *Mater. Today Phys.* **21**, 100548 (2021).
- [54] S. Toth and B. Lake, Linear spin wave theory for single- Q incommensurate magnetic structures, *J. Phys.: Condens. Matter* **27**, 166002 (2015).

- [55] J.-i. Igarashi, $1/S$ expansion for thermodynamic quantities in a two-dimensional Heisenberg antiferromagnet at zero temperature, *Phys. Rev. B* **46**, 10763 (1992).
- [56] A. V. Syromyatnikov, Collective excitations in spin- $\frac{1}{2}$ magnets through bond-operator formalism designed both for paramagnetic and ordered phases, *Phys. Rev. B* **98**, 184421 (2018).
- [57] A. V. Syromyatnikov, Multiple magnon modes in spin- $\frac{1}{2}$ Heisenberg antiferromagnet on simple square lattice in strong magnetic field, *Phys. Rev. B* **102**, 014409 (2020).
- [58] M. Moretti Sala, V. Schnell, S. Boseggia, L. Simonelli, A. Al-Zein, J. G. Vale, L. Paolasini, E. C. Hunter, R. S. Perry, D. Prabhakaran, A. T. Boothroyd, M. Krisch, G. Monaco, H. M. Rønnow, D. F. McMorrow, and F. Mila, Evidence of quantum dimer excitations in $\text{Sr}_3\text{Ir}_2\text{O}_7$, *Phys. Rev. B* **92**, 024405 (2015).
- [59] H. Katsura, N. Nagaosa, and P. A. Lee, Theory of the Thermal Hall Effect in Quantum Magnets, *Phys. Rev. Lett.* **104**, 066403 (2010).
- [60] R. Shindou, R. Matsumoto, S. Murakami, and J.-i. Ohe, Topological chiral magnonic edge mode in a magnonic crystal, *Phys. Rev. B* **87**, 174427 (2013).
- [61] A. Mook, J. Henk, and I. Mertig, Edge states in topological magnon insulators, *Phys. Rev. B* **90**, 024412 (2014).
- [62] K. A. van Hoogdalem, Y. Tserkovnyak, and D. Loss, Magnetic texture-induced thermal Hall effects, *Phys. Rev. B* **87**, 024402 (2013).
- [63] J. Romhányi, K. Penc, and R. Ganesh, Hall effect of triplons in a dimerized quantum magnet, *Nat. Commun.* **6**, 6805 (2015).